Climatic controls on watermass chemistry in a Paleocene lacustrine setting, Subei Basin, Eastern China

Yang Liu[a, b*], Lu Yun[c], Zhijun Jin[d], XiPeng He [c], Yuqiao Gao[c], Ling Zan[c], Caixia Hua[c], Xuan Tang[b*], Rui Zhang[d], Simon W. Poulton[e]

[a] *College of Environmental Science and Engineering, Dalian Maritime University, Dalian 116026, China.*

[b] *School of Energy Resource, China University of Geosciences (Beijing), Beijing 100083, China.*

[c] *Sinopec East China Oil and Gas Company, Nanjing 210000, China.*

[d] *Institute of Energy, Peking University, Beijing 100871, China.*

[e] *School of Earth and Environment, University of Leeds, Leeds LS2 9JT, UK.*

Corresponding Authors: Yang Liu (yang.liu@dlmu.edu.cn); Xuan Tang (tangxuan@cugb.edu.cn)

ABSTRACT

The Paleocene Epoch was characterized by global climate fluctuations and major carbon cycle perturbations. During the greenhouse climate that characterized the early Cenozoic, a short-lived late Paleocene global cooling event has been recognized from marine records. However, the response of the terrestrial system to this climate cooling event is poorly understood. Here, we present major and trace element analyses, iron speciation systematics, carbonate carbon isotope data, and mineralogical observations for lacustrine sediments from Member II of the Paleocene Funing Formation (E_1f_2), utilizing well-preserved drill core from the Subei Basin, Eastern China. Both chemical (chemical index of alteration, Al/K ratios) and mineralogical (mineralogical index of alteration, clay/feldspar ratios) proxies yield consistent weathering and paleoclimatic interpretations, suggesting a transition from cool and arid climatic conditions to warmer and more humid climatic conditions. Correlation of carbon isotopes between the Subei Basin and deep-sea records implies that this terrestrial setting records the short-lived Paleocene climate cooling event. The combination of climate records and paleosalinity proxies (B/Ga and S/TOC) indicates a relatively high salinity water column (brackish to saline) under cool and arid climatic conditions in the Subei Basin, suggesting that elevated salinity was likely produced via net-evaporative conditions, rather than marine incursions. A shift toward less saline brackish conditions up-section reflects an increase in precipitation and freshwater runoff under warmer and more humid climatic conditions. Iron speciation and redox-sensitive trace metal systematics reveal fluctuating redox conditions, from oxic through to anoxic ferruginous, but with the distinct development of better ventilated conditions as freshwater

inputs increased under more humid conditions. Our findings demonstrate the sensitivity of terrestrial climate to the late Paleocene climate cooling event, and further reveal the chemical response of a lacustrine setting to a cooling episode in a greenhouse world.

Key words: Paleoclimate; Salinity; Redox; Paleocene; Subei Basin.

INTRODUCTION

The Paleocene Epoch (66–56 Ma) was bookended by the extreme biological and climatic events associated with the Cretaceous–Paleogene (K–Pg) mass extinction and the Paleocene–Eocene Thermal Maximum (PETM) (Hollis et al., 2022). In addition, the Paleocene was characterized by a series of climatic oscillations superimposed on the long-term early Cenozoic warming trend (Zachos et al., 2001, 2008; Hollis et al., 2022). In the greenhouse world of the early Cenozoic, however, a short-lived cooling event has been identified in New Zealand and in the southwest Pacific during the late Paleocene (~60–58 Ma; Hollis et al., 2014, 2022; Bijl et al., 2021). The TEX_{86} sea surface temperature (SST) proxy at mid-Waipara River and ODP Sites 1172 and 1121 indicates a cooling of ~2–6°C (Hollis et al., 2014; Bijl et al., 2021), while the MBT′–CBT mean annual air temperature (MAAT) proxy records ~2°C of cooling (Hollis et al., 2014). The regional cooling inferred from the southwest Pacific SST and MAAT proxies is consistent with a positive excursion in deep-sea benthic foraminiferal oxygen isotope ($\delta^{18}O$) records (Cramer et al., 2011; Barnet et al., 2019; Westerhold et al., 2020). In addition, physiognomic analysis of leaf fossils from Paleocene sites in western and eastern South Island (Kennedy, 2003), as well

as pollen assemblages from ODP Site 1172 (Contreras et al., 2014), provide further evidence for a pronounced cooling event. This late Paleocene cooling has been linked to drawdown of atmospheric CO_2 (Hollis et al., 2022), likely due to both reduced volcanic CO_2 emissions (Westerhold et al., 2011) and increased organic carbon burial due to tectonism (Kurtz et al., 2003).

Significantly, the late Paleocene climate cooling event correlates with the initial stages (~59.3–58.2 Ma) of the Paleocene carbon isotope maximum (PCIM) at ~59.3–57.4 Ma (Corfield and Cartlidge, 1992; Thompson and Schmitz, 1997; Hollis et al., 2005, 2014, 2022). This positive carbon isotope excursion (CIE) is recorded in bulk marine carbonate and bulk organic carbon, and is generally considered to represent an episode of enhanced organic carbon burial, leading to regionally widespread deposition of organic-rich marine sediments (Hollis et al., 2014, 2022). Enhanced organic carbon burial during the late Paleocene climate cooling event may have been driven by either increased marine productivity as a result of enhanced ocean circulation (Corfield and Cartlidge, 1992; Thompson and Schmitz, 1997), or an increased input of terrestrial organic matter as a consequence of eustatic sea-level fall and elevated coastal erosion (Hilting et al., 2008; Schiøler et al., 2010; Hollis et al., 2014, 2022). However, the existing signals for this climate cooling event are largely derived from marine records at mid and high latitudes, while mid-low latitude terrestrial climate records are scarce. In addition, the response of watermass chemistry in terrestrial settings is unclear.

Here, we present high-resolution total organic carbon (TOC) data, carbonate carbon ($\delta^{13}C_{carb}$) and bulk organic carbon ($\delta^{13}C_{org}$) isotope data, iron speciation systematics, and

89 mineralogical and elemental data for lacustrine sediments from Member II of the Paleocene
90 Funing Formation (E_1f_2) in the mid-low latitude Subei Basin, Eastern China. These
91 chemical and mineralogical proxies are utilized to reconstruct chemical weathering
92 intensity and paleoclimatic conditions during deposition of E_1f_2, which together with the
93 high-resolution $\delta^{13}C$ data, allow the identification of a potential record of the late Paleocene
94 climate cooling event in the terrestrial Subei Basin. In addition, a combination of both
95 salinity and redox proxy data provides detailed constraints on watermass chemistry. Hence,
96 our new geochemical data provide insight into the terrestrial response to an episode of
97 global cooling during the late Paleocene.
98

99 ## GEOLOGICAL BACKGROUND

100 The Subei Basin is a large, lacustrine rift basin that was developed on the northern
101 margin of the Lower Yangtze Block in eastern China (Fig. 1). Since the Late Cretaceous,
102 this basin has been affected by two major rifting episodes that were accompanied by
103 thermal subsidence (Liu et al., 2017). Paleomagnetic results reveal that the Subei Basin
104 was at mid-low latitudes in the early Paleocene, with a paleolatitude of ~32–33°N (Boucot
105 et al., 2009), similar to today. During the Paleocene and earliest Eocene, thousands of
106 meters of fluvio-lacustrine sediments were deposited, which comprise the four members of
107 the Funing Formation (Fig. 1). In ascending order, Member I (E_1f_1) mainly consists of
108 continental red beds, comprising interbedded fine-grained sandstones, siltstones and
109 mudstones. Member II (E_1f_2) is composed mainly of dark gray mudstones. Member III (E_1f_3)
110 consists mainly of interbedded fine-grained sandstones and mudstones, followed by basal

Eocene mudstones of Member IV (E_1f_4) (Qiu et al., 2006).

Our study utilizes samples from drill core QY 1, located in the Qintong Depression of the Subei Basin, which preserves a relatively continuous record of E_1f_2 deposited in a deep lacustrine setting (Fig. 1). Three main lithofacies are present, including laminated dolomitic mudstones, massive calcareous mudstones and mudstones, with wavy, laminated dolomitic mudstones dominating in the studied core. Thin sections show well-developed horizontal laminae and clear laminar boundaries (Fig. 2A). Lighter laminae are mainly composed of quartz and micritic dolomite and calcite, while darker counterparts are mainly composed of clay and organic matter (Fig. 2B). The massive calcareous mudstone is mostly homogeneous and contains scattered monocrystalline quartz grains (Fig. 2E). Carbonate occurs in the form of cryptocrystalline cement in mudstone. A grayish black or dark gray massive mudstone lithofacies is developed mainly towards the top of E_1f_2 in drill core QY 1. Fragments of ostracods are commonly observed in this lithofacies (Fig. 2F), and the lack of wavy laminae or bedding suggests a deeper water environment than the underlying dolomitic mudstones.

MATERIALS AND METHODS

Prior to geochemical analyses, bulk rock samples were carefully trimmed to avoid veins, possible weathered surfaces and visible pyrite nodules or bands. Approximately 100 g of each sample was crushed to powder (~200 mesh) using an agate mortar. All geochemical analyses were conducted at the State Key Laboratory of Biogeology and Environmental Geology, China University of Geosciences (Wuhan), or at SINOPEC East China Oil and

Gas Company Experimental Research Center.

Total organic carbon (TOC) and sulfur (TS) concentrations were measured using a 902 T carbon-sulfur analyzer. For TOC analyses, ~2 g of sample powder was first treated with 4 M HCl for 24 h to remove inorganic carbon. Analytical precision was better than 0.2 wt.% based on replicate analyses of Alpha Resources standard AR4007 (total carbon = 7.62 wt.%). Bulk organic carbon isotopes ($\delta^{13}C_{org}$) were analyzed using an elemental analyzer (EA) coupled to a Delta V Advantage isotope ratio mass spectrometer. Two international reference standards, USGS40 ($\delta^{13}C$ = –26.39‰) and IVA-Urea ($\delta^{13}C$ = –37.32‰), were used for calibration. Results are reported in per mil notation relative to Vienna Pee Dee Belemnite (VPDB), and analytical precision was better than 0.2‰ (1σ) based on replicate analyses of standards.

For carbonate $\delta^{13}C$ and $\delta^{18}O$ analyses, about 50–300 μg of dried sample powder was reacted with 100% phosphoric acid at 70°C. The resulting CO_2 was introduced into a MAT 253 isotope ratio mass spectrometer for isotopic measurements. The $\delta^{13}C$ and $\delta^{18}O$ data were calibrated relative to international reference standard NBS-19 ($\delta^{13}C$ = +1.95‰; $\delta^{18}O$ = −2.20‰) and Chinese national standard GBW04416 ($\delta^{13}C$ = +1.61‰; $\delta^{18}O$ = −11.59‰). Results are reported in permil notation relative to the Vienna Pee Dee Belemnite (VPDB), with a precision of better than ± 0.1‰ (1σ).

For major element analyses, approximately 1 g of dried sample powder was mixed with lithium borate and fused into glass disks, and then determined via X-ray fluorescence spectrometry (PANalytical Epsilon 3X). The analytical precision was better than 5% (1σ) based on replicate analyses of standards (BCR-1, COQ-1, GSR-5 and GSR-6). For trace

element analyses, approximately 50 mg of sample powder was digested with 1 ml HF and 1 ml HNO_3 in Teflon bombs at 190°C for over 48 h. About 1–2 ml $HClO_4$ was added to the sample solutions to aid oxidation of organic matter. The final solutions were diluted with 2% HNO_3 and analyzed using an Agilent 7700x inductively coupled plasma mass spectrometer (ICP-MS). Analytical precision was better than 5% (1σ) based on replicate analyses of standards (AGV-2, BCR-2, GSR-1 and GSR-6). For B concentration analyses, ~100 mg of sample powder was weighed into a 15 ml crucible and mixed with ~100 mg of a buffering agent. The buffering agent was a mixture of $K_2S_2O_7$, NaF, Al_2O_3, carbon powder, and GeO_2 in the ratio of 22:20:43:14:0.007 (Cheng et al., 2021). The concentrations of B were analyzed using an AES-8000 Emission Spectrometer (Beijing Beifen-Ruili Analytical Instrument Co. Ltd.), with an analytical precision of better than 1% based on replicate analyses of standards GBW 07304 and GBW 07307.

The chemical index of alteration (CIA) is expressed as: CIA = molar $[(Al_2O_3)/(Al_2O_3 + CaO^* + Na_2O + K_2O)] \times 100$, where CaO* represents the CaO content of the silicate fraction only (Nesbitt and Young, 1982). CaO* was corrected using available P_2O_5 data (CaO* = mole CaO − mole $P_2O_5 \times 10/3$). If the remaining number of moles is higher than that of Na_2O, then CaO* is assumed to be equivalent to Na_2O. Otherwise, the CaO value was adopted as the CaO* value (McLennan, 1993). The redox-sensitive trace metals (RSTMs) Mo, U, V and Mn are displayed as enrichment factors (EFs), which were calculated as: $X_{EF} = (X/Al)_{sample}/(X/Al)_{UCC}$, where X is the trace element of interest and the subscripts 'sample' and 'UCC' refer to the studied sample and upper continental crust (Rudnick and Gao, 2003), respectively.

All samples analyzed in this study have total Fe concentrations >0.5 wt.%, and are therefore considered suitable for palaeoredox interpretation via Fe speciation (Clarkson et al., 2014). Four pools that together comprise highly reactive Fe (Fe_{HR}) were determined, including Fe bound in carbonates (Fe_{carb}), ferric (oxyhydr)oxides (Fe_{ox}), magnetite (Fe_{mag}) and pyrite (Fe_{Py}). Fe_{Py} was calculated stoichiometrically by the content of pyrite sulfur extracted following the chromium reduction method (Canfield et al., 1986). The other three Fe species (i.e., Fe_{carb}, Fe_{ox} and Fe_{mag}) were determined via the operationally-defined sequential extraction procedure of Poulton and Canfield (2005). First, approximately 100 mg of sample powder was subjected to 10 ml of 1 mol/L sodium acetate solution (pH = 4.5 with acetic acid) for 48 h at 50°C, for the extraction of Fe_{carb}. The sample residue was then leached in 10 ml of a 50 g/L sodium dithionite and 0.2 mol/L sodium citrate solution (adjusted to pH 4.8 with acetic acid) for 2 h at room temperature, in order to extract Fe_{ox}. Finally, the sample residue was treated with ammonium oxalate solution (10 ml of a 0.17 mol/L oxalic acid and 0.2 mol/L ammonium oxalate solution) for 6 h at room temperature, to extract Fe_{mag}. All extraction solutions were diluted 100-fold with 2% HNO_3 before analysis by atomic absorption spectroscopy (AAS). The analytical precision for each fraction was within 5%, based on replicate analyses of the international Fe speciation standard, WHIT (Alcott et al., 2020).

Mineral compositions were determined using X-ray diffraction (XRD) on a Bruker D8 Advance X-ray diffractometer with Cu-Kα radiation. The samples were analyzed at 40 kV and 30 mA, and the stepwise scanning measurements were performed at a rate of 4°/min in the range of 3° to 85° (2θ). The relative mineral proportions were estimated from the

areas of their major peaks with Lorentz polarization correction.

RESULTS

All geochemical data are provided in Supplementary Table S1. The $\delta^{13}C_{carb}$ values exhibit an increasing trend up-section (Fig. 3E), with variable $\delta^{13}C_{carb}$ values from −6.6‰ to +4.3‰ (mean = +0.8 ± 1.9‰) below 3750 m, and less variable values from +0.4‰ to +4.1‰ above 3750 m (mean = +2.0 ± 0.8‰). The CIA data, Al/K ratios, mineralogical index of alteration (MIA) values (calculated as MIA = [quartz/(quartz+plagioclase+K-feldspar)] × 100; Rieu et al., 2007), and clay/feldspar proxies all exhibit a similar first-order trend, with lower values below 3750 m and elevated values above (Fig. 4). CIA values below 3750 m range from 42 to 64 (mean = 52 ± 5), Al/K values range from 2.3 to 4.3 (mean = 2.9 ± 0.3), MIA values range from 32 to 87 (mean = 63 ± 9), and clay/feldspar ratios range from 0.2 to 8.8 (mean = 2.5 ± 1.5). Samples above 3750 m have CIA values ranging from 62 to 72 (mean = 67 ± 3), Al/K values ranging from 3.5 to 4.6 (mean = 4.2 ± 0.3), MIA values ranging from 72 to 92 (mean = 87 ± 4), and clay/feldspar ratios ranging from 2.0 to 13.4 (mean = 8.0 ± 2.9). The $\delta^{13}C_{org}$ values exhibit an overall decreasing trend with a significant negative shift at ~3750 m (Fig. 4F). Below 3750 m, $\delta^{13}C_{org}$ values range from −28.2‰ to −25.3‰ (mean = −27.2 ± 0.6‰). Above 3750 m, $\delta^{13}C_{org}$ values decrease to a range of −29.3‰ to −27.9‰ (mean = −28.4 ± 0.4‰).

Samples below 3750 m in drill core QY 1 generally have relatively lower TOC concentrations, ranging from 0.17 to 3.27 wt.% (mean = 1.05 ± 0.58 wt.%; Fig. 5). Total sulfur in this interval shows some variability, ranging from 0.02 to 2.70 wt.% (mean = 0.86

± 0.42 wt.%; Fig. 5). Above 3750 m, TOC is more enriched, with values varying between 0.70 to 4.06 wt.% (mean = 2.24 ± 0.59 wt.%), while TS ranges from 0.29 to 1.21 wt.% (mean = 0.62 ± 0.27 wt.%). B/Ga and S/TOC ratios show a shift to lower values at ~3750 m (Fig. 5). Below 3750 m, B/Ga ratios range from 3.6 to 8.6 (mean = 6.2 ± 1.4) and S/TOC ratios range from 0.02 to 3.75 (mean = 1.07 ± 0.76). Above 3750 m, B/Ga ratios decrease to a range of 3.3 to 5.5 (mean = 4.3 ± 0.7) and S/TOC ratios decrease to a range of 0.12 to 0.67 (mean = 0.30 ± 0.16). Iron speciation reveals little significant change up-section, with Fe_{HR}/Fe_T and Fe_{Py}/Fe_{HR} values ranging from 0.28 to 0.91 (mean = 0.54 ± 0.10) and from 0.01 to 0.62 (0.37 ± 0.13), respectively (Fig. 6). The exception to this concerns two samples towards the top of the succession, which have lower Fe_{HR}/Fe_T ratios.

We identify three general zones based on a combined evaluation of RTSM enrichment factors (Fig. 6). From the base of E_1f_2 to ~3890 m, Mo_{EF} values are commonly >1 and show considerable scatter (1.89 ± 1.08), while U_{EF} (1.05 ± 0.20), V_{EF} (1.14 ± 0.24) and Mn_{EF} (1.06 ± 0.27) show less scatter, with average values close to 1. From ~3890 to ~3750 m, Mo_{EF} (1.69 ± 0.81) and U_{EF} (0.99 ± 0.22) values remain similar to lower in the succession, but V_{EF} values show more scatter, with an overall increase to 1.41 ± 0.30. In this zone, Mn_{EF} values are also generally similar to lower in the section (1.09 ± 0.76), but with some elevated values (Fig. 6). Above ~3750 m, Mo_{EF} (1.83 ± 0.55) and V_{EF} (1.43 ± 0.35) values are similar to the preceding zone. By contrast, U_{EF} values transition to levels significantly below 1, while Mn_{EF} values initially transition to high levels (up to ~6), followed by a decrease to values close to 1 (Fig. 6).

DISCUSSION

Evaluation of diagenetic alteration

Burial diagenesis may potentially alter the carbon isotope signature of authigenic carbonate (e.g., Garzione et al., 2004). Here, we evaluate the extent of diagenetic alteration using sedimentary and geochemical approaches. Petrographic analyses of typical samples reveal that these rocks are mudstones with a homogeneous fine-grained micritic matrix. Furthermore, the carbonate crystals are generally less than 2 μm in size and show little evidence for more coarsely crystalline phases associated with recrystallization (Fig. 2D). These petrographic features suggest that carbonates in drill core QY 1 have undergone limited diagenetic alteration.

Strontium is rapidly lost during post-depositional diagenesis, and hence Sr concentrations and Mn/Sr ratios have been widely used to evaluate the degree of carbonate diagenesis (Brand and Veizer, 1980, Banner and Hanson, 1990). The oxygen isotope composition of carbonate rocks is also considered a sensitive indicator for diagenetic alteration (Banner and Hanson, 1990). Generally, carbonates that experienced a high degree of diagenetic alteration tend to yield elevated Mn/Sr ratios, low Sr concentrations and low $\delta^{18}O$ values (e.g., Marshall, 1992; Kaufman et al., 1993). In drill core QY 1, all samples generally exhibit elevated Sr concentrations (>300 ppm) and low Mn/Sr ratios (<4; the majority of samples (94%) have Mn/Sr ratios <2), while $\delta^{18}O$ values are higher than −10‰ (Table S1). Samples from the massive mudstone lithofacies have relatively low Sr concentrations and elevated Mn/Sr ratios due to their low carbonate content. In addition, no apparent correlation exists between $\delta^{13}C_{carb}$ values and Sr

concentrations (R^2 = 0.08), Mn/Sr ratios (R^2 = 0.10), Mg/Ca ratios (R^2 = 0.17) or $\delta^{18}O$ values (R^2 = 0.05) (Fig. S1). These characteristics are consistent with well-preserved carbonate rocks that have undergone minimal diagenetic alteration (Banner and Hanson, 1990), suggesting that the $\delta^{13}C_{carb}$ values obtained in this study likely track the isotopic signal of dissolved inorganic carbon (DIC) in lake water.

Recognition of the PCIM and terrestrial climate cooling in the Subei Basin

Given the absence of volcanic horizons for isotopic dating, we employed biostratigraphic dating and carbon isotope stratigraphy to document the PCIM in drill core QY 1. Studies on fossil charophytes, ostracods and sporo-pollen suggest that the Funing Formation in the Subei Basin is Paleocene in age (Wang et al., 2019). The *Homoeucypris bucerusa-Parailyocypris chngzhouensis-Candona (Lineocypris) acclina* ostracod assemblage found in E_1f_2 in the Gaoyou Depression of the Subei Basin assigns this member to the late Paleocene (Zhu et al., 2004; Wang et al., 2019). Furthermore, the *Pentapollenites-Rhoipites-Ephedripites-Cedripites* pollen assemblage found in the same member in the Gaoyou Depression is consistent with early paleontological investigations in the Subei Basin, indicating a mid−late Paleocene age (Qian et al., 1993; Zhu et al., 2004).

Carbon isotope excursions have proven to be a useful tool for global chronostratigraphic correlation (Cramer and Jarvis, 2020). The carbon isotope composition of lake water is controlled by a variety of factors, including inputs from rivers and rainfall, evaporation, CO_2 exchange between lake water and the atmosphere, and the balance between primary production and respiration within the lake (e.g., Carroll and Bohacs, 1999; Leng and

287 Marshall, 2004). As a result, the $\delta^{13}C$ values of lacustrine carbonate reflect the average
288 isotope composition of DIC in the lake system with varying degrees of equilibrium with
289 atmospheric CO_2 (Bade et al., 2004). Since the overall inflow/outflow balance of lakes is
290 closely related to global and regional climate change, and most of the processes are
291 associated with atmospheric CO_2, carbon isotope values for lacustrine carbonate have
292 been used as a tool for reconstructing paleoenvironments and paleoclimates (e.g., Leng
293 and Marshall, 2004). Carbon isotope excursions in lacustrine carbonates are often
294 comparable to those in marine carbonates because both are associated with global
295 changes to the carbon cycle, and hence lacustrine carbon isotope values have been used
296 to track global carbon cycle perturbations (e.g., Chen et al., 2014).

297 The PCIM is an ~2 Ma episode that has been well documented in deep-sea benthic
298 foraminifera and bulk marine carbonates (ODP Site 1209 and ODP Site 1262), with $\delta^{13}C$
299 values reaching a Cenozoic maximum (Barnet et al., 2019; Westerhold et al., 2020; Hollis
300 et al., 2022). Hence, we compared the carbon isotope excursions observed in the Subei
301 Basin with marine records to identify the PCIM in the late Paleocene based on the following
302 criteria. First, our diagenetic evaluation suggests that the $\delta^{13}C_{carb}$ results from the Subei
303 Basin have not been significantly affected by diagenetic alteration. Second, the $\delta^{13}C_{carb}$
304 excursions in the Subei Basin were assigned to those in marine records if they occurred at
305 approximately the same time period and appeared in the same trend.

306 Five positive $\delta^{13}C_{carb}$ excursions (P1 to P5) and three negative $\delta^{13}C_{carb}$ excursions (N1
307 to N3) are identified in the study profile, and the carbon isotope variations observed in the
308 Subei Basin are strikingly consistent with those in the marine realm (Fig. 3). The first and

second positive $\delta^{13}C_{carb}$ excursions (P1 and P2) in core QY 1, as well as the negative $\delta^{13}C_{carb}$ excursion (N1) between them (Fig. 3E), are comparable with $\delta^{13}C$ excursions in marine records between ~59−58.7 Ma (Fig. 3D). The third and fourth positive $\delta^{13}C_{carb}$ excursions (P3 and P4), as well as the negative $\delta^{13}C_{carb}$ excursion (N2), then correspond to the $\delta^{13}C$ excursions between ~58.5 and 58.3 Ma. The third negative $\delta^{13}C_{carb}$ excursion (N3) consists of two small negative $\delta^{13}C_{carb}$ shifts, followed by a positive $\delta^{13}C_{carb}$ excursion (P5) in the study core, which is consistent with marine records between ~58.2 and 58.0 Ma. The unnamed "*" event (58.15 Ma) in marine records (Barnet et al., 2019) most likely corresponds to the onset of the P5 at ~3750 m in core QY 1. Thus, the isotopic trends we observe in the Subei Basin appear to mirror marine records between ~59 and 58 Ma. Although the lack of a detailed age control prevents a fully conclusive interpretation of the terrestrial carbon isotope record, it appears highly likely that the Subei Basin records the PCIM.

Having established that the PCIM is likely documented in core QY 1, we next explore the regional terrestrial response to this climate cooling event. The CIA is a widely used proxy for reconstructing paleoclimatic conditions via changes in chemical weathering intensity (Nesbitt and Young, 1982). High CIA values reflect the enhanced removal of mobile cations during chemical weathering under humid and warm climate conditions. By contrast, low CIA values indicate the near absence of chemical weathering and consequently reflect cool and/or arid conditions (Nesbitt and Young, 1982). Generally, CIA values of between 50 and 65 represent an arid climate with low chemical weathering intensity, values of 65–85 indicate a temperate climate with moderate chemical weathering,

and values >85 reflect a hot and humid climate with strong chemical weathering (Nesbitt and Young, 1982; Bahlburg and Dobrzinski, 2011). However, diagenetic K-metasomatism (conversion of kaolinite to illite) should be taken into consideration when calculating CIA values for fine-grained sediments (Fedo et al., 1995). The extent of K-metasomatism can be identified using an Al_2O_3–CaO* + Na_2O–K_2O (A–CN–K) ternary diagram (Fedo et al., 1995). Our samples exhibit a simple weathering trend roughly parallel to the A-CN boundary (Fig. S2), suggesting limited K-metasomatism. Furthermore, studies have shown that the influence of K-metasomatism on first-order CIA trends is not apparent, even in Neoproterozoic and early Cambrian sedimentary rocks (Rieu et al., 2007; Zhai et al., 2018). Additionally, CIA values may be influenced by the provenance composition and lithological changes. However, there is no significant correlation between CIA values and provenance indicators (e.g., Al/Ti, Th/Sc; Fig. S3) (Taylor and McLennan, 1985; McLennan, 1993), and the trends in CIA do not coincide with strong lithological or facies changes (Fig. 4), which together suggest that the first-order trends in CIA values most parsimoniously represent changes in the intensity of chemical weathering.

Chemical weathering intensity can also be inferred from the ratio of non-mobile elements to mobile elements (e.g., Al/K) during weathering (Gaillardet et al., 1999; Garzanti et al., 2014), with higher values indicating greater depletion of mobile elements and thus stronger chemical weathering intensity. The mineralogical index of alteration (MIA) is sensitive to the intensity of chemical weathering, since it reflects the relative concentrations of stable quartz versus unstable feldspars, and is largely unaffected by sorting or abrasion (Nesbitt et al., 1996; Rieu et al., 2007). Higher MIA values reflect substantial loss of feldspar relative

353 to quartz due to intense chemical weathering under warm and humid conditions, while
354 lower values indicate minimal weathering under cool and/or arid conditions. In addition, an
355 increase in the ratio of clay minerals to feldspar can be a direct indication of enhanced
356 chemical weathering, as some clay minerals are formed by the decomposition of feldspar
357 (Chamley, 1989).

358 The similar first-order trends observed between these independent chemical and
359 mineralogical proxies (Fig. 4) supports a robust paleoclimate signal. Samples below 3750
360 m are characterized by relatively low CIA (52 ± 5), Al/K (2.9 ± 0.3, clustering around 3),
361 MIA (63 ± 9, clustering around 60) and clay/feldspar (2.5 ± 1.5, mostly <5) values, indicating
362 low chemical weathering intensity in the source region, under a relatively cold and arid
363 climate. By contrast, the concurrent increase in CIA (67 ± 3), Al/K (4.2 ± 0.3), MIA (87 ± 4)
364 and clay/feldspar (8.0 ± 2.9) values above 3750 m suggests enhanced chemical
365 weathering intensity under temperate conditions. This terrestrial climate reconstruction
366 (below 3750 m) is therefore consistent with marine records, where both the TEX_{86} and
367 MBT′–CBT proxies suggest ~2–6°C of cooling (Hollis et al., 2014, 2022; Fig. 3C).
368 Furthermore, the climate cooling recorded in drill core QY 1 also occurs within the
369 Paleocene oxygen isotope maximum (POIM) at ~59.6–58.2 Ma, and the positive shift in
370 benthic foraminiferal $\delta^{18}O$ suggests global cooling of deep waters (Hollis et al., 2022; Fig.
371 3B). Notably, the climatic transition at ~3750 m in drill core QY 1 appears to represent the
372 termination of this short-lived cooling event, consistent with that observed in marine
373 records. Indeed, the "*" event coincides with the termination of the POIM and climate
374 cooling, followed by a warming trend in the late Paleocene (Hollis et al., 2022; Fig. 3B),

suggesting that the "*" event marks a significant turning point in Paleocene climate. This climate transition, in turn, provides additional constraints on carbon isotope correlations between the Subei Basin and the marine realm. Specifically, the carbon isotope curves and climate records below 3750 m in drill core QY 1 correspond to the lower part of the PCIM associated with the POIM and climate cooling, while those above 3750 m correspond to the upper part of the PCIM associated with climate warming (Hollis et al., 2022; Fig. 3).

The late Paleocene cooling event has been linked to a short-lived drawdown in atmospheric CO_2 levels (Hollis et al., 2022). This hypothesis can be tested by the $\delta^{13}C_{org}$ values in drill core QY 1, because a decline in atmospheric CO_2 would result in ^{13}C enrichment in the biomass of algae (Freeman and Hayes, 1992), as well as in C_3 plants (Schubert and Jahren, 2012). Previous organic geochemical and organic petrological investigations on mudstones in drill core QY 1 indicate that organic matter mainly comprises type II kerogen and derives from algae (Zan et al., 2023). Thus, relatively higher $\delta^{13}C_{org}$ values (−27.2 ± 0.6‰) below 3750 m in drill core QY 1 may suggest lower atmospheric CO_2 levels, while a shift towards lower $\delta^{13}C_{org}$ values (−28.4 ± 0.4‰) above 3750 m represents an increase in CO_2 levels (Fig. 4F). A significant negative $\delta^{13}C_{org}$ excursion at ~3750 m is consistent with the climate transition suggested by paleoclimate proxies. Although not quantitative, the trends in atmospheric CO_2 levels inferred from our $\delta^{13}C_{org}$ data are broadly consistent with those revealed by quantitative estimates of atmospheric CO_2 concentrations in the late Paleocene (Hollis et al., 2022). Overall, the observed similarity between the paleoenvironmental records of the Subei Basin and marine settings demonstrates the sensitivity of mid-low latitude terrestrial regions to global climate

fluctuations during the late Paleocene.

Watermass salinity

Paleo-watermass salinity is evaluated using B/Ga and S/TOC ratios (Berner and Raiswell, 1984; Wei and Algeo, 2020). B/Ga ratios are a potential proxy for paleosalinity due to the much higher concentrations of B in seawater relative to freshwater, in addition to the strong potential for adsorption of B by clay minerals (Dominik and Stanley, 1993). By contrast, Ga mainly exists in detrital silicate minerals and is generally depleted in seawater compared to freshwater (Chen et al., 1997). Although not highly quantitative, recent work on modern sediments has suggested that B/Ga ratios of <3, 3–6 and >6 are indicative of freshwater, brackish and marine settings, respectively (Wei and Algeo, 2020). Sediment S/TOC ratios can also provide useful paleosalinity information (Berner and Raiswell, 1984). Although S/TOC ratios may also be influenced by redox conditions, productivity levels, sulfate concentrations and diagenesis, modern sediment studies have suggested that S/TOC ratios of <0.1 and >0.1 are indicative of freshwater and brackish to marine settings, respectively (Wei and Algeo, 2020).

In drill core QY 1, samples below 3750 m generally exhibit elevated B/Ga ratios (6.2 ± 1.4), with samples dominantly plotting in the upper brackish or marine regions. By contrast, all B/Ga ratios above 3750 m occur within the range of 3–6 (4.3 ± 0.7), consistent with persistent brackish conditions (Fig. 5). The S/TOC profile is broadly consistent with this salinity interpretation, whereby the majority of samples below 3750 m have S/TOC values significantly greater than 0.1 (1.1 ± 0.8), indicating brackish to marine conditions. Above

this depth, the decline in S/TOC ratios to 0.3 ± 0.2 supports a reduction in watermass salinity (Fig. 5). In this analysis, we excluded the use of Sr/Ba ratios for paleosalinity because the presence of carbonate-hosted Sr commonly results in elevated bulk-rock Sr/Ba ratios (Wei and Algeo, 2020). Indeed, there is a positive correlation (R^2 = 0.60) between Sr and CaO contents in our samples. Furthermore, Sr/Ba ratios are generally low and show no correlation with CaO (R^2 = 0.07) in the <4 wt.% CaO interval, but Sr/Ba ratios rise significantly and show a positive correlation with CaO when CaO concentrations are >4 wt.% (Fig. S4).

Redox reconstruction

We next use independent paleo-redox proxies to constrain bottom-water redox conditions in the Subei Basin. However, we first note the potential complications when using these proxies in lacustrine systems. With regard to Fe speciation, boundaries for distinguishing oxic (Fe_{HR}/Fe_T <0.22) and anoxic (Fe_{HR}/Fe_T >0.38) water column redox conditions were devised for marine settings (Raiswell and Canfield, 1998; Poulton and Raiswell, 2002; Raiswell et al., 2001; Raiswell et al., 2018). Indeed, it is well established that Fe_{HR}/Fe_T ratios in riverine particulates reflect the intensity of chemical weathering in the source region (Canfield, 1997; Poulton and Raiswell, 2002; Poulton and Canfield,2005), with a global average, discharge-weighted Fe_{HR}/Fe_T ratio of 0.43 ± 0.03 (Poulton and Raiswell, 2002). The global river particulate flux has an elevated Fe_{HR}/Fe_T ratio relative to marine sediments due to the preferential trapping of riverine Fe_{HR} in proximal environments (e.g., flood plains, estuaries, fjords, salt marshes; Poulton and Raiswell, 2002). As a result,

441 care is required when applying marine sediment Fe speciation thresholds to lacustrine
442 sediments. However, this approach can be successfully used, particularly in larger
443 lacustrine settings (such as the Subei Basin) where the Fe shuttle that leads to Fe_{HR}
444 enrichments under anoxic water conditions (Raiswell and Canfield, 1998; Anderson and
445 Raiswell, 2004; Severmann et al., 2008) may still operate (e.g., Cumming et al., 2013).
446 In the case of the Subei Basin, the low intensity chemical weathering indicated by our
447 data also supports the applicability of Fe speciation systematics, since under such
448 conditions it is unlikely that Fe_{HR}/Fe_T ratios were high in the sediment supplied to the basin
449 (Canfield, 1997; Poulton and Raiswell, 2002), suggesting that a false anoxic signal is
450 unlikely. Indeed, Fe_{HR}/Fe_T ratios are dominantly considerably elevated in core QY 1,
451 relative to the average composition of riverine particulates (Fig. 6), which in such a low
452 chemical weathering setting implies water column mobilization and deposition of Fe_{HR}
453 under anoxic conditions (Raiswell and Canfield, 1998; Poulton and Raiswell, 2002). Low
454 Fe_{Py}/Fe_{HR} ratios (<0.6; Fig. 6) then suggest that when anoxic, the water column was
455 ferruginous rather than euxinic (Poulton et al., 2004; Poulton and Canfield, 2011; Poulton,
456 2021).
457 To provide further support and insight into the evolution of water column redox conditions,
458 we also utilize RSTM systematics. Vanadium is soluble under oxic conditions and is
459 commonly transported to sediments as the vanadate ion ($H_2V(VI)O_4^-$) adsorbed onto Mn
460 oxides. However, during the reduction of Mn oxides under dysoxic conditions, V may be
461 released from sediments, whereas under anoxic conditions, the vanadate released during
462 Mn oxide reduction is reduced to the vanadyl ion ($V(IV)O_2^+$), which is highly surface-

463 reactive and tends to be retained in the sediment (Emerson and Huested, 1991). Thus, the
464 behaviour of Mn and V are linked, but in addition, significant enrichments in Mn can occur
465 as a result of precipitation of Mn oxides during intervals of water column oxygenation (Tebo
466 et al., 2004), although direct precipitation of Mn carbonates may also occur under anoxic
467 conditions (Wittkop et al., 2020).

468 Molybdenum is transported to the ocean as the molybdate anion, and moderate
469 sediment enrichments can occur during uptake by Fe (oxyhydr)oxide minerals formed in
470 ferruginous settings (e.g., Algeo and Tribovillard, 2009; Tribovillard et al., 2012; Li et al.,
471 2023). By contrast, under high concentrations of H_2S, particle-reactive thiomolybdate forms
472 (Helz et al., 1996), leading to increased Mo enrichments in the sediments (Emerson and
473 Huested, 1991; Helz et al., 1996; Erickson and Helz, 2000). Uranium is preferentially buried
474 in sediments deposited beneath anoxic bottom waters regardless of whether euxinic or
475 ferruginous conditions dominate, as U reduction primarily occurs in the sediments
476 (Anderson et al., 1989; Klinkhammer and Palmer, 1991).

477 As with Fe speciation, however, care needs to be taken when utilizing RSTMs in a closed
478 lacustrine system such as the Subei Basin, due to the potential for low sediment
479 enrichments under anoxic conditions as a result of limited resupply of RSTMs (e.g.,
480 Tribovillard et al., 2012). An additional issue concerns defining baseline regional RSTM
481 concentrations in sediments deposited under oxic conditions, such that anoxia can be
482 identified by relative sediment enrichments (e.g., Algeo and Li, 2020; Li et al., 2023). Here,
483 we note that two samples towards the top of the succession (at ~3686 m) display robust
484 evidence for deposition under oxic conditions, with low Fe_{HR}/Fe_T ratios occurring coincident

485 with low RSTM values (Fig. 6). For these samples, while V_{EF} values remain elevated
486 (potentially due to anoxic conditions during diagenesis, rather than anoxia in the water
487 column), Mo_{EF} and Mn_{EF} values fall close to 1, suggesting that this value suitably reflects
488 the composition of the background sediment influx. However, U_{EF} values are considerably
489 lower than 1 (average = 0.47), suggesting that the source material was low in U (e.g., Li et
490 al., 2023). Hence, a U_{EF} value of 0.47 appears to provide a more robust reflection of the
491 sediment supplied to the basin, and hence values significantly above this likely reflect
492 deposition under anoxic conditions.

493 Based on a combined evaluation of the RSTM and Fe speciation profiles, we identify
494 three distinct intervals characterized by differing redox conditions. From the base of E_1f_2 to
495 ~3890 m, Fe_{HR}/Fe_T enrichments occur alongside moderate (i.e., typical of a restricted
496 basinal setting; see above), but fluctuating enrichments in Mo and U, while V_{EF} and Mn_{EF}
497 values are dominantly close to 1 (Fig. 6). We interpret this combined signal to reflect an
498 unstable water column, with fluctuations between dysoxic and anoxic ferruginous
499 conditions, whereby the former would limit enrichments in V and Mn, while the latter would
500 result in enrichments in Fe_{HR}/Fe_T, Mo (via uptake to Fe (oxyhydr)oxide minerals) and U. A
501 similar signal is apparent from ~3890 to 3750 m (Fig. 6), but V enrichments are significantly
502 enhanced, suggesting that anoxia was more prevalent through this interval. Above 3750
503 m, as the water column freshened as climate warmed (Figs. 4 and 5), high Mn_{EF} values
504 initially occur in the calcareous mudstone, before a decrease in the overlying massive
505 mudstone, coincident with an overall decrease in Fe_{HR}/Fe_T ratios and decreased U_{EF} and
506 Mo_{EF} values (Fig. 6). We interpret this to reflect a transition to better oxygenated conditions

(although redox conditions may still have fluctuated), which initially resulted in drawdown of mobilized Mn from the water column. Subsequently, since the sedimentological features suggest that the massive mudstone reflects deeper water deposition relative to the underlying dolomitic mudstone (see above), enhanced ventilation of deeper waters is indicated.

Climate driven variations in watermass chemistry

Over longer timescales, watermass salinity largely depends on overall water balance (i.e., meteoric precipitation and runoff versus evaporation) and the degree of watermass exchange with the open ocean, both of which are typically related to climatic changes (Matthias and Godfrey, 1994; Michener et al., 1997). The brackish to near-fully marine salinities recorded below 3750 m could potentially have resulted from marine incursions, which have been linked to the development of many salinized lacustrine systems, such as the Eocene Bohai Bay Basin (e.g., Wei et al., 2018). Indeed, it has been proposed that the lacustrine Subei Basin may have experienced marine incursions during deposition of the Funing Formation, based on the fossil record (e.g., fossil tubes) and mineralogical evidence (Yu and Wang, 1981; Qiu et al., 2006). However, a recent detailed investigation of tube-dominated bioherms in E_1f_2 in the Subei Basin has led to their reinterpretation as fully lacustrine caddisfly larval cases, which occur together with abundant non-marine algae as well as freshwater ostracods, gastropods and conchostracans, suggesting that E_1f_2 was most likely deposited in a lacustrine setting that was not subject to significant marine incursions (Zhou et al., 2020). Furthermore, the late Paleocene climate cooling

529 event corresponds to a global fall in sea level (Kominz et al., 2008; Harris et al., 2010;
530 Cramer et al., 2011; Hollis et al., 2014), which would have been expected to limit the
531 seawater influx into the Subei Basin.

532 The degree of watermass restriction can be further assessed based on Mo-TOC
533 relationships and Co x Mn values. In modern marine environments, Mo/TOC ratios are
534 generally high under unrestricted conditions (e.g., ~45 ± 5 for Saanich Inlet), while Mo/TOC
535 ratios are low under restricted watermass conditions (e.g., 4.5 ± 1 for the Black Sea) (Algeo
536 and Lyons, 2006). In addition, modern upwelling environments typically have sedimentary
537 Co x Mn values below 0.4, with values exceeding 0.4 in restricted environments (Sweere
538 et al., 2016). Deposition of E_1f_2 in a highly restricted basin is also supported by consistently
539 low Mo/TOC ratios (1.74 ± 1.46) and Co x Mn values (0.91 ± 0.65) in excess of 0.4 (Fig.
540 7).

541 Alternatively, hypersaline lakes can potentially develop under arid climatic conditions, in
542 which evaporation exceeds precipitation (Hardie et al., 2009). This scenario is more in line
543 with the climate records we observe in the Subei Basin. Below 3750 m, the overall low
544 paleoclimate proxy values are correlated with elevated paleosalinity proxy values,
545 suggesting that limited precipitation and freshwater runoff under a cool and arid climate
546 may have led to a net-evaporative condition, and thus increased watermass salinity (Figs.
547 8 and 9A). A shift towards less saline conditions above 3750 m was likely the result of
548 enhanced precipitation and freshwater runoff under warmer and more humid climatic
549 conditions, as indicated by elevated paleoclimate proxy values and decreased paleosalinity
550 proxy values (Figs. 8 and 9B). We note that below 3750 m in drill core QY 1, an increase

551 in CIA values is associated with an increase in B/Ga ratios (Fig. 8). One possible
552 explanation is that lacustrine systems may be particularly sensitive to climate fluctuations,
553 and thus intermittent warming in a predominantly arid climate (all samples below 3750 m
554 have CIA values <65) may have led to intensified evaporation, resulting in an increase in
555 salinity.

556 Under cool and arid climatic conditions, a reduction in freshwater runoff would have
557 promoted a salinity-stratified watermass, which would have restricted water column mixing,
558 thereby promoting the development of oxygen-depleted deeper waters (Figs. 8 and 9A).
559 This would have occurred beneath oxic surface waters, which is supported by the presence
560 of fishbone fossils (Fig. 2C). Under warmer and more humid climatic conditions (i.e., above
561 3750 m in drill core QY 1), the increased freshwater runoff and lower overall salinity
562 appears to have promoted enhanced ventilation of deeper waters (Figs. 8 and 9B),
563 although redox conditions may have continued to fluctuate, and our data cannot confirm
564 whether the deepest basinal waters also became oxygenated. In summary, our data
565 suggest that the observed variability in watermass salinity and redox conditions in the
566 Subei Basin were closely linked to climate fluctuations.

567

568 ## CONCLUSIONS

569 This study reports a new geochemical dataset for lacustrine mudstones from Member II
570 of the Paleocene Funing Formation (E_1f_2) in the Subei Basin, Eastern China. Chemical
571 (CIA, Al/K) and mineralogical (MIA, clay/feldspar) paleoclimate proxies suggest a shift in
572 climatic conditions during deposition of E_1f_2, with predominantly cool and arid climatic

conditions below 3750 m giving way to warmer and more humid climatic conditions above. This climate change record, along with a compelling carbon isotope correlation between the Subei Basin and deep-sea records, suggests that the sediments document a terrestrial system response to the short-lived late Paleocene climate cooling event. Paleosalinity proxies (B/Ga and S/TOC) demonstrate a major change in salinity coincident with the change in paleoclimate, from brackish/near-fully marine salinity conditions under cool and arid conditions, to less saline conditions under a warmer and more humid climate. This suggests that elevated salinity was likely due to net-evaporative conditions, rather than marine incursions, whereas the reduced salinity up-section reflects enhanced precipitation and freshwater runoff. Redox proxies (iron speciation and redox-sensitive trace metal systematics) reveal dynamic redox conditions, from dysoxic to anoxic ferruginous during the cooling event, to better ventilated conditions as the water column freshened. These findings suggest that terrestrial water column settings were sensitive to the global climate fluctuations of the late Paleocene, and provide an example of the response of lacustrine watermass chemistry to a cooling episode in a greenhouse world.

ACKNOWLEDGMENTS

This work was supported by the National Natural Science Foundation of China (42102171, 42372164, 41972132), the Fundamental Research Funds for the Central Universities (3132023518). We would like to thank the two anonymous reviewers for their constructive and insightful comments that significantly improved the manuscript.

DATA ACCESSIBILITY STATEMENT

The original data generated in this study are provided in the Supplemental Material (Table S1).

REFERENCES CITED

Alcott, L. J., Krause, A. J., Hammarlund, E. U., Bjerrum, C. J., Scholz, F., Xiong, Y., Hobson, A. J., Neve, L., Mills, B. J. W., Marz, C., Schnetger, B., Bekker, A., and Poulton, S. W., 2020, Development of Iron Speciation Reference Materials for Palaeoredox Analysis: Geostandards and Geoanalytical Research, v. 44, p. 581–591.

Algeo, T. J., and Li, C., 2020, Redox classification and calibration of redox thresholds in sedimentary systems: Geochimica et Cosmochimica Acta, v. 287, p. 8–26.

Algeo, T.J., and Lyons, T.W., 2006, Mo–total organic carbon covariation in modern anoxic marine environments: Implications for analysis of paleoredox and paleohydrographic conditions: Paleoceanography, v. 21, p. 204–230.

Algeo, T. J., and Tribovillard, N., 2009, Environmental analysis of paleoceanographic systems based on molybdenum-uranium covariation: Chemical Geology, v. 268, p. 211–225.

Anderson, R. F., Fleisher, M. Q., and Lehuray, A. P. J. G. E. C. A., 1989, Concentration, oxidation state, and particulate flux of uranium in the Black Sea: Geochimica et Cosmochimica Acta, v. 53, p. 2215–2224.

Anderson, T. F., and Raiswell, R., 2004, Sources and mechanisms for the enrichment of highly reactive iron in euxinic Black Sea sediments: American Journal of Science, v. 304, p. 203–233.

Bade, D.L., Carpenter, S.R., Cole, J.J., Hanson, P.C., and Hesslein, R.H., 2004, Controls of $\delta^{13}C$–DIC

617 in lakes: Geochemistry, lake metabolism, and morphometry: Limnology and Oceanography, v.
618 49, p. 1160–1172.
619 Bahlburg, H., and Dobrzinski, N. J. G. S. L. M., 2009, A review of the Chemical Index of Alteration (CIA)
620 and its application to the study of Neoproterozoic glacial deposits and climate transitions:
621 Geological Society London Memoirs, v. 36, p. 81–92.
622 Banner, J. L., and Hanson, G. N. J. G. E. C. A., 1990, Calculation of simultaneous isotopic and trace
623 element variations during water-rock interaction with applications to carbonate diagenesis:
624 Geochimica et Cosmochimica Acta, v. 54, p. 3123–3137.
625 Barnet, J. S. K., Littler, K., Westerhold, T., Kroon, D., Leng, M. J., Bailey, I., Roehl, U., and Zachos, J.
626 C., 2019, A High-Fidelity Benthic Stable Isotope Record of Late Cretaceous-Early Eocene
627 Climate Change and Carbon-cycling: Paleoceanography and Paleoclimatology, v. 34, p. 672–
628 691.
629 Berner, R. A., and Raiswell, R. J. G., 1984, C/S method for distinguishing freshwater from marine
630 sedimentary rocks: Geology, v. 12, p. 365–368.
631 Bijl, P. K., Frieling, J., Cramwinckel, M. J., Boschman, C., Sluijs, A., and Peterse, F., 2021,
632 Maastrichtian–Rupelian paleoclimates in the southwest Pacific–a critical re-evaluation of
633 biomarker paleothermometry and dinoflagellate cyst paleoecology at Ocean Drilling Program
634 Site 1172: Climate of the Past, v. 17, p. 2393–2425.
635 Boucot, A. J., Chen, X., Scotese, C.R., Fan, J.X., 2009, Phanerozoic Global Climatic Reconstruction,
636 China [in Chinese with English Abstract]: Science Press.
637 Brand, U., and Veizer, J. J. J. o. S. R., 1980, Chemical diagenesis of a multicomponent carbonate
638 system; 1, Trace elements: Journal of Sedimentary Research, v. 50, p. 1219–1236.

639 Canfield, D. E., 1997, The geochemistry of river particulates from the continental USA: Major elements:
640 Geochimica et Cosmochimica Acta, v. 61, p. 3349–3365.
641 Canfield, D. E., Raiswell, R., Westrich, J. T., Reaves, C. M., and Berner, R. A. J. C. G., 1986, The use
642 of chromium reduction in the analysis of reduced inorganic sulfur in sediments and shales:
643 Chemical Geology, v. 54, p. 149–155.
644 Carroll, A.R., and Bohacs, K.M., 1999, Stratigraphic classification of ancient lakes: balancing tectonic
645 and climatic controls: Geology, v. 27, p. 99–102.
646 Chamley, H., 1989, Clay Sedimentology, Springer-Verlag: Berlin.
647 Chen, Z. Y., Chen, Z. L., and Zhang, W. G., 1997, Quaternary stratigraphy and trace-element indices of
648 the Yangtze delta, eastern China, with special reference to marine transgressions: Quaternary
649 Research, v. 47, p. 181–191.
650 Chen, Z., Wang, X., Hu, J., Yang, S., Zhu, M., Dong, X., Tang, Z., Peng, P., and Ding, Z., 2014, Structure
651 of the carbon isotope excursion in a high-resolution lacustrine Paleocene-Eocene Thermal
652 Maximum record from central China: Earth and Planetary Science Letters, v. 408, p. 331–340.
653 Cheng, M., Zhang, Z., Algeo, T. J., Liu, S., Liu, X., Wang, H., Chang, B., Jin, C., Pan, W., Cao, M., and
654 Li, C., 2021, Hydrological controls on marine chemistry in the Cryogenian Nanhua Basin (South
655 China): Earth-Science Reviews, v. 218, p. 103678.
656 Clarkson, M. O., Poulton, S. W., Guilbaud, R., and Wood, R. A., 2014, Assessing the utility of Fe/Al and
657 Fe-speciation to record water column redox conditions in carbonate-rich sediments: Chemical
658 Geology, v. 382, p. 111–122.
659 Contreras, L., Pross, J., Bijl, P. K., O'Hara, R. B., and Brinkhuis, H. J. C. o. t. P., 2014, Southern high-
660 latitude terrestrial climate change during the Paleocene-Eocene derived from a marine pollen

661 record (ODP Site 1172, East Tasman Plateau): Climate of the Past, v. 10, p. 1401–1420.
662 Corfield, R. M., and Cartlidge, J. E. J. T. N., 1992, Oceanographic and climatic implications of the
663 Palaeocene carbon isotope maximum: Terra Nova, v. 4, no. 4.
664 Cramer, B. D., and Jarvis, I. J. G. T. S., 2020, Carbon isotope stratigraphy. In: Geologic Time Scale, pp.
665 309–343.
666 Cramer, B. S., Miller, K. G., Barrett, P. J., and Wright, J. D., 2011, Late Cretaceous-Neogene trends in
667 deep ocean temperature and continental ice volume: Reconciling records of benthic
668 foraminiferal geochemistry ($\delta^{18}O$ and Mg/Ca) with sea level history: Journal of Geophysical
669 Research-Oceans, v. 116, p. C12023.
670 Cumming, V. M., Poulton, S. W., Rooney, A. D., and Selby, D., 2013, Anoxia in the terrestrial
671 environment during the late Mesoproterozoic: Geology, v. 41, p. 583–586.
672 Dominik, J., and Stanley, D. J. J. C. G., 1993, Boron, beryllium and sulfur in Holocene sediments and
673 peats of the Nile delta, Egypt: Their use as indicators of salinity and climate, v. 104, p. 203–216.
674 Emerson, S. R., Huested, S.S., 1991, Ocean anoxia and the concentrations of molybdenum and
675 vanadium in seawater: Marine Chemistry, v. 34, p. 177–196.
676 Erickson, B. E., and Helz, G. R. J. G. E. C. A., 2000, Molybdenum (VI) speciation in sulfidic waters:
677 Stability and lability of thiomolybdates, v. 64, p. 1149–1158.
678 Fedo, C. M., Nesbitt, H. W., and Young, G. M. J. G., 1995, Unraveling the effects of potassium
679 metasomatism in sedimentary rocks and paleosols, with implications for paleoweathering
680 conditions and provenance: Geology, v. 23, p. 921–924.
681 Gaillardet, J., Dupré, B., and Allègre, C. J., 1999, Geochemistry of large river suspended sediments:
682 Silicate weathering or recycling tracer? Geochimica et Cosmochimica Acta, v. 63, p. 4037–4051.

683 Garzanti, E., Padoan, M., Setti, M., Lopez-Galindo, A., and Villa, I. M., 2014, Provenance versus
684 weathering control on the composition of tropical river mud (southern Africa): Chemical Geology,
685 v. 366, p. 61–74.
686 Garzione, C. N., Dettman, D. L., and Horton, B. K., 2004, Carbonate oxygen isotope paleoaltimetry:
687 evaluating the effect of diagenesis on paleoelevation estimates for the Tibetan plateau:
688 Palaeogeography Palaeoclimatology Palaeoecology, v. 212, p. 119–140.
689 Hardie, L. A., Smoot, J. P., Eugster, H. P. J. M., and Sediments, A. L., 1978, Saline Lakes and their
690 Deposits: A Sedimentological Approach, p. 7–41.
691 Harris, A. D., Miller, K. G., Browning, J. V., Sugarman, P. J., Olsson, R. K., Cramer, B. S., and Wright, J.
692 D., 2010, Integrated stratigraphic studies of Paleocene-lowermost Eocene sequences, New
693 Jersey Coastal Plain: Evidence for glacioeustatic control: Paleoceanography, v. 25, p. PA3211.
694 Helz, G. R., Miller, C. V., Charnock, J. M., Mosselmans, J. F. W., Pattrick, R. A. D., Garner, C. D., and
695 Vaughan, D. J., 1996, Mechanism of molybdenum removal from the sea and its concentration
696 in black shales: EXAFS evidence: Geochimica et Cosmochimica Acta, v. 60, p. 3631–3642.
697 Hilting, A. K., Kump, L. R., and Bralower, T. J., 2008, Variations in the oceanic vertical carbon isotope
698 gradient and their implications for the Paleocene-Eocene biological pump: Paleoceanography,
699 v. 23, p. PA3222.
700 Hollis, C. J., Dickens, G. R., Field, B. D., Jones, C. M., and Strong, C. P., 2005, The Paleocene-Eocene
701 transition at Mead Stream, New Zealand: a southern Pacific record of early Cenozoic global
702 change: Palaeogeography Palaeoclimatology Palaeoecology, v. 215, p. 313–343.
703 Hollis, C. J., Naeher, S., Clowes, C. D., Naafs, B. D. A., Pancost, R. D., Taylor, K. W. R., Dahl, J., Li, X.,
704 Ventura, G. T., and Sykes, R., 2022, Late Paleocene CO_2 drawdown, climatic cooling and

terrestrial denudation in the southwest Pacific: Climate of the Past, v. 18, p. 1295–1320.

Hollis, C. J., Tayler, M. J. S., Andrew, B., Taylor, K. W., Lurcock, P., Bijl, P. K., Kulhanek, D. K., Crouch, E. M., Nelson, C. S., Pancost, R. D., Huber, M., Wilson, G. S., Ventura, G. T., Crampton, J. S., Schioler, P., and Phillips, A., 2014, Organic-rich sedimentation in the South Pacific Ocean associated with Late Paleocene climatic cooling: Earth-Science Reviews, v. 134, p. 81–97.

Kaufman, A. J., Jacobsen, S. B., Knoll, A. H. J. E., and Letters, P. S., 1993, The Vendian record of Sr and C isotopic variations in seawater: Implications for tectonics and paleoclimate, v. 120, p. 409–430.

Kennedy, E. M., 2003, Late Cretaceous and Paleocene terrestrial climates of New Zealand: leaf fossil evidence from South Island assemblages: New Zealand Journal of Geology and Geophysics, v. 46, p. 295–306.

Klinkhammer, G. P., and Palmer, M. R. J. G. c. a., 1991, Uranium in the oceans: Where it goes and why, v. 55, p. 1799–1806.

Kominz, M. A., Browning, J. V., Miller, K. G., Sugarman, P. J., Mizintseva, S., and Scotese, C. R., 2008, Late Cretaceous to Miocene sea-level estimates from the New Jersey and Delaware coastal plain coreholes: an error analysis: Basin Research, v. 20, p. 211–226.

Kurtz, A. C., Kump, L. R., Arthur, M. A., Zachos, J. C., and Paytan, A., 2003, Early Cenozoic decoupling of the global carbon and sulfur cycles: Paleoceanography, v. 18, p. 1090.

Leng, M.J., and Marshall, J.D., 2004, Palaeoclimate interpretation of stable isotope data from lake sediment archives: Quaternary Science Reviews, v. 23, p. 811–831.

Li, S., Wignall, P. B., Xiong, Y., and Poulton, S. W., 2023, Calibration of redox thresholds in black shale: Insight from a stratified Mississippian basin with warm saline bottom waters: Geological Society

of America Bulletin. DOI: https://doi.org/10.1130/B36915.1

Liu, Y., Chen, Q., Wang, X., Hu, K., Cao, S., Wu, L., and Gao, F., 2017, Influence of normal fault growth and linkage on the evolution of a rift basin: A case from the Gaoyou depression of the Subei Basin, eastern China: AAPG Bulletin, v. 101, p. 265–288.

Marshall, J D., 1992, Climatic and oceanographic isotopic signals from the carbonate rock record and their preservation: Geological Magazine, v. 129, p. 143–160.

Matthias, T., Godfrey, J.S., 1994, Regional Oceanography: An Introduction: Pergamon.

McLennan, S. M., 1993, Weathering and global denudation: Journal of Geology, v. 101, p. 295–303.

Michener, W. K., Blood, E. R., Bildstein, K. L., Brinson, M. M., and Gardner, L. R., 1997, Climate change, hurricanes and tropical storms, and rising sea level in coastal wetlands: Ecological Applications, v. 7, p. 770–801.

Nesbitt, H. W., Young, G. M., McLennan, S. M., and Keays, R. R., 1996, Effects of chemical weathering and sorting on the petrogenesis of siliciclastic sediments, with implications for provenance studies: Journal of Geology, v. 104, p. 525–542.

Nesbitt, H. W., and Young, G. M. J. N., 1982, Early Proterozoic climates and plate motions inferred from major element chemistry of lutites: Nature, v. 299, p. 715–717.

Poulton, S. W, Fralick, P. & Canfield, D., 2004, The transition to a sulphidic ocean ~ 1.84 billion years ago: Nature, v. 431, p. 173–177.

Poulton, S. W., 2021, The Iron Speciation Paleoredox Proxy: Elements in Geochemical Tracers in Earth System Science, Cambridge University Press.

Poulton, S. W., and Canfield, D. E., 2011, Ferruginous Conditions: A Dominant Feature of the Ocean through Earth's History: Elements, v. 7, p. 107–112.

749 Poulton, S. W., and Canfield, D. E. J. C. G., 2005, Development of a sequential extraction procedure
750 for iron: implications for iron partitioning in continentally derived particulates: Geological
751 Magazine, v. 214, p. 209–221.
752 Poulton, S. W., and Raiswell, R., 2002, The low-temperature geochemical cycle of iron: From continental
753 fluxes to marine sediment deposition: American Journal of Science, v. 302, p. 774–805.
754 Qian, Z., Zheng, Y., Song, Z., 1993, Spores and pollen grains from Funing Group of northern Jiangsu
755 [in Chinese with English Abstract]: Acta Palaeontologica Sinica, v. 32, p. 49–63.
756 Qiu, X., Liu, Y., Fu, Q., 2006, Sequence Stratigraphy and Depositional Evolution of the Subei Basin from
757 the Late Cretaceous to the Tertiary [in Chinese with English Abstract]: Geological Publishing
758 House, p. 154.
759 Raiswell, R., and Canfield, D. E., 1998, Sources of iron for pyrite formation in marine sediments:
760 American Journal of Science, v. 298, p. 219–245.
761 Raiswell, R., Hardisty, D. S., Lyons, T. W., Canfield, D. E., Owens, J. D., Planavsky, N. J., Poulton, S.
762 W., and Reinhard, C. T., 2018, The iron paleoredox proxies: a guide to the pitfalls, problems and
763 proper practice: American Journal of Science, v. 318, p. 491–526.
764 Raiswell, R., Newton, R., and Wignall, P. B., 2001, An indicator of water-column anoxia: Resolution of
765 biofacies variations in the Kimmeridge Clay (Upper Jurassic, UK): Journal of Sedimentary
766 Research, v. 71, p. 286–294.
767 Rieu, R., Allen, P. A., Ploetze, M., and Pettke, T., 2007, Climatic cycles during a Neoproterozoic
768 "snowball" glacial epoch: Geology, v. 35, p. 299–302.
769 Rudnick, R. L., Gao, S., 2003, Composition of the continental crust. In: Rudnick RL (ed) The crust:
770 Holland HD, Turekian KK (eds) Treatise on geochemistry, Oxford.

771 Schioler, P., Rogers, K., Sykes, R., Hollis, C. J., Ilg, B., Meadows, D., Roncaglia, L., and Uruski, C.,
772 2010, Palynofacies, organic geochemistry and depositional environment of the Tartan Formation
773 (Late Paleocene), a potential source rock in the Great South Basin, New Zealand: Marine and
774 Petroleum Geology, v. 27, p. 351–369.
775 Severmann, S., Lyons, T. W., Anbar, A., McManus, J., and Gordon, G., 2008, Modern iron isotope
776 perspective on the benthic iron shuttle and the redox evolution of ancient oceans: Geology, v.
777 36, p. 487–490.
778 Sweere, T., Boorn, S.V.D., Dickson, A.J., and Reichart, G.J., 2016, Definition of new tracemetal proxies
779 for the controls on organic matter enrichment in marine sediments based on Mn, Co, Mo and
780 Cd concentrations: Chemical Geology, v. 441, p. 235–245.
781 Taylor, S. R., and McLennan, S.M., 1985, The Continental Crust: its Composition and Evolution:
782 Blackwell Scientific Publications.
783 Tebo, B. M., Bargar, J. R., Clement, B. G., Dick, G. J., Murray, K. J., Parker, D., Verity, R., and Webb,
784 S. M., 2004, Biogenic manganese oxides: Properties and mechanisms of formation: Annual
785 Review of Earth and Planetary Sciences, v. 32, p. 287-328.
786 Thompson, E. I., and Schmitz, B., 1997, Barium and the late Paleocene $\delta^{13}C$ maximum: evidence of
787 increased marine surface productivity: Paleoceanography, v. 12, p. 239–254.
788 Tribovillard, N., Algeo, T. J., Lyons, T., and Riboulleau, A., 2006, Trace metals as paleoredox and
789 paleoproductivity proxies: An update: Chemical Geology, v. 232, p. 12–32.
790 Wang, Y., Li, Q., Bai, B., Jin, X., Mao, F., and Meng, J., 2019, Paleogene integrative stratigraphy and
791 timescale of China: Science China-Earth Sciences, v. 62, p. 287–309.
792 Wei, W., and Algeo, T. J., 2020, Elemental proxies for paleosalinity analysis of ancient shales and

mudrocks: Geochimica et Cosmochimica Acta, v. 287, p. 341–366.

Wei, W., Algeo, T. J., Lu, Y., Lu, Y., Liu, H., Zhang, S., Peng, L., Zhang, J., and Chen, L., 2018, Identifying marine incursions into the Paleogene Bohai Bay Basin lake system in northeastern China: International Journal of Coal Geology, v. 200, p. 1–17.

Westerhold, T., Marwan, N., Drury, A. J., Liebrand, D., Agnini, C., Anagnostou, E., Barnet, J. S. K., Bohaty, S. M., De Vleeschouwer, D., Florindo, F., Frederichs, T., Hodell, D. A., Holbourn, A. E., Kroon, D., Lauretano, V., Littler, K., Lourens, L. J., Lyle, M., Palike, H., Rohl, U., Tian, J., Wilkens, R. H., Wilson, P. A., and Zachos, J. C., 2020, An astronomically dated record of Earth's climate and its predictability over the last 66 million years: Science, v. 369, p. 1383–1387.

Westerhold, T., Roehl, U., Donner, B., McCarren, H. K., and Zachos, J. C., 2011, A complete high-resolution Paleocene benthic stable isotope record for the central Pacific (ODP Site 1209): Paleoceanography, v. 26, p. PA2216.

Wittkop, C., Swanner, E. D., Grengs, A., Lambrecht, N., Fakhraee, M., Myrbo, A., Bray, A. W., Poulton, S. W., and Katsev, S., 2020, Evaluating a primary carbonate pathway for manganese enrichments in reducing environments: Earth and Planetary Science Letters, v. 538, p. 116201.

Yu, C., Wang, H., 1981, Some tube-like fossils from the Early Tertiary of Northern Jiangsu [in Chinese with English abstract]: Acta Palaeontologica Sinica, v. 20, p. 406–417.

Zachos, J., Pagani, M., Sloan, L., Thomas, E., and Billups, K., 2001, Trends, rhythms, and aberrations in global climate 65 Ma to present: Science, v. 292, p. 686–693.

Zachos, J. C., Dickens, G. R., and Zeebe, R. E., 2008, An early Cenozoic perspective on greenhouse warming and carbon-cycle dynamics: Nature, v. 451, p. 279–283.

Zan, L., Bai, L., Yin, Y., and Zhang, W., 2023, Basic characteristics and genesis analysis of shale oil in

the second member of Paleogene Funing Formation in Qintong Sag, Subei Basin [in Chinese with English abstract]: Petroleum Geology and Experiment, v. 45, p. 356–365.

Zhai, L., Wu, C., Ye, Y., Zhang, S., and Wang, Y., 2018, Fluctuations in chemical weathering on the Yangtze Block during the Ediacaran-Cambrian transition: Implications for paleoclimatic conditions and the marine carbon cycle: Palaeogeography Palaeoclimatology Palaeoecology, v. 490, p. 280–292.

Zhou, X., Jiang, Z., and MacEachern, J. A., 2020, Criteria for differentiating microbial-caddisfly bioherms from those of marine polychaetes in a lacustrine setting: Paleocene second member, Funing Formation, Subei Basin, East China: Palaeogeography Palaeoclimatology Palaeoecology, v. 560, p. 109974.

Zhu, Y.,Yan, S., and Yang, X., 2004, The upper cretaceous to paleogene micropalaeontological stratigraphy and palaeoenvironment of the well d1 in the gaoyou depression, northern jiangsu basin [in Chinese with English abstract]: Acta Micropalaeontologica Sinica, v. 21, p. 267–272.

FIGURE CAPTIONS

Figure 1. Location map and stratigraphy of drill core QY 1. (A) Tectonic location of the Subei Basin on the Yangtze Block (Zhou et al., 2020) and the location of the investigated drill core. The grey box represents the location of the Lower Yangtze Block. (B) Stratigraphy of the Subei basin (Zhou et al., 2020) showing the stratigraphic column for drill core QY 1.

Figure 2. Photographs of Member II of the Paleocene Funing Formation (E_1f_2) in the Subei

837 Basin from drill core QY 1. (A) Core photograph at 3924.3 m showing laminated dolomitic
838 mudstone with well-developed laminae and clear laminae boundaries. (B) Laminated
839 dolomitic mudstone (4031.6 m) with well-preserved light quartz-dolomite-calcite mixed
840 laminae and dark organic-rich laminae. (C) Sample of laminated dolomitic mudstone with
841 well-preserved fishbone fossils (3859.4 m). (D) Scanning electron microscope (SEM)
842 image showing fine-grained dolomite (Dol) crystals in laminated dolomitic mudstone (3853
843 m). (E) Sample of massive calcareous mudstone containing scattered monocrystalline
844 quartz grains (3730 m). (F) Sample of massive mudstone with well-preserved ostracod
845 fragments (3698 m).
846
847 Figure 3. Paleocene carbon and oxygen isotope, and temperature records. (A) Trends in
848 benthic foraminiferal and bulk carbonate carbon isotopes (Barnet et al., 2019; Westerhold
849 et al., 2020; Hollis et al., 2022). (B) Trends in benthic foraminiferal oxygen isotopes (Barnet
850 et al., 2019; Westerhold et al., 2020; Hollis et al., 2022). (C) Temperatures estimated from
851 the TEX_{86}^{H} sea surface temperature (SST) proxy and the MBT′–CBT mean annual air
852 temperature (MAAT) proxy, adapted from the compilation of Hollis et al. (2014, 2022).
853 Carbon isotope correlation between marine records (D) and the Subei Basin (E) during the
854 Paleocene carbon isotope maximum (PCIM).
855
856 Figure 4. Variations in chemical (A−B) and mineralogical (C−D) paleoclimate proxies,
857 $\delta^{13}C_{carb}$ and $\delta^{13}C_{org}$ values (E−F) in drill core QY 1. CIA = chemical index of alteration, and
858 MIA = mineralogical index of alteration. The dashed line at 65 on the CIA plot represents

the approximate boundary between low intensity chemical weathering under an arid climate (<65), and moderate chemical weathering under a temperate climate (65-85; Nesbitt and Young, 1982; Bahlburg and Dobrzinski, 2011). The horizontal dashed line represents a depth of ~3750 m in drill core QY 1.

Figure 5. Stratigraphic distribution of TOC (A) and TS (B) concentrations, and the paleosalinity proxies B/Ga (C) and S/TOC (D) in drill core QY 1. B/Ga and S/TOC salinity facies thresholds from Wei and Algeo (2020). Horizontal dashed line represents a depth of ~3750 m in drill core QY 1.

Figure 6. Stratigraphic distribution of redox proxy data for drill core QY 1, including Fe speciation systematics (A−B), Mo (C), U (D), V (E) and Mn (F) enrichment factors. Vertical dashed lines on the Fe_{HR}/Fe_T plot represent the boundaries for distinguishing oxic, equivocal and anoxic water column conditions in marine settings (Poulton and Canfield, 2011), while the grey bar represents the global average for riverine particles (Poulton and Raiswell, 2002). Dashed lines on the Fe_{Py}/Fe_{HR} plot represent the calibrated boundaries for distinguishing ferruginous, equivocal and euxinic conditions for anoxic samples (Poulton, 2021). Dashed lines at a value of 1 on the enrichment factor plots (C-F) represent the crustal average. Additional dashed line at 0.47 on the U_{EF} plot (D) represents the estimated oxic baseline value for this core (see text for details). Horizontal dashed line represents a depth of ~3750 m in drill core QY 1.

Figure 7. Total organic carbon (TOC) versus Mo (A) and TOC versus Co × Mn (B) for the samples from drill core QY 1. Dashed lines on A represent different modern marine systems (Cariaco Basin, Framvaren Fjord, and Black Sea) with variable hydrographic restriction conditions (Algeo and Lyons, 2006). Dashed line on B represents a cut-off value of 0.4 for the distinction between open/upwelling (<0.4) and restricted settings (>0.4) (Sweere et al., 2016).

Figure 8. Variation in $\delta^{13}C_{carb}$, $\delta^{13}C_{org}$, TOC, CIA, B/Ga and Mn_{EF} values plotted against age for drill core QY 1. The age model used here is based on carbon isotope correlation between drill core QY 1 and marine records. Horizontal dashed line represents a depth of ~3750 m in drill core QY 1, which corresponds to the "*" event (Horizontal purple solid line) identified in marine records.

Figure 9. Schematic showing the evolution of watermass chemistry in the lacustrine Subei Basin under arid (A) and humid (B) climatic conditions.

Figure S1. Crossplots of Sr versus $\delta^{13}C_{carb}$ (A), Mn/Sr versus $\delta^{13}C_{carb}$ (B), Mg/Ca versus $\delta^{13}C_{carb}$ (C), and $\delta^{18}O$ versus $\delta^{13}C_{carb}$ (D).

Figure S2. A–CN–K (Al_2O_3–CaO* + Na_2O–K_2O) ternary diagram of the samples from drill core QY 1. CIA–Chemical Index of Alteration, Pl–plagioclase, Kfs–K-feldspar, Sm–

smectite, Kln–kaolinite, Chl–chlorite, Ms–muscovite.

Figure S3. Crossplots of Al/Ti versus CIA (A) and Th/Sc versus CIA (B).

Figure S4. Crossplots of CaO versus Sr (A) and CaO versus Sr/Ba (B).

[1]Supplemental Material. *[Table S1 and Figures S1–S4]* Please visit https://doi.org/10.1130/XXXX to access the supplemental material, and contact editing@geosociety.org with any questions.

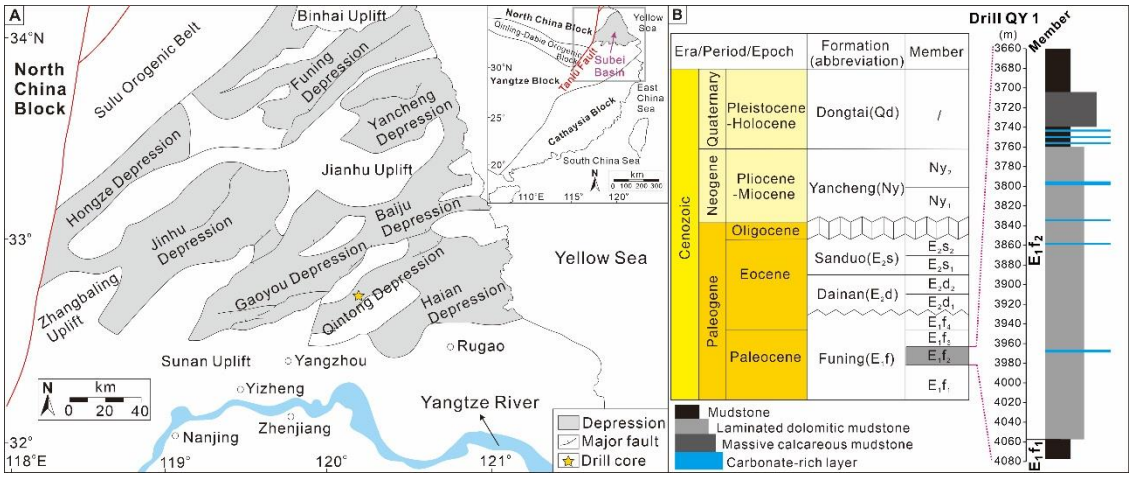
A
34°N
North China Block
Sulu Orogenic Belt
Binhai Uplift
Funing Depression
Yancheng Depression
Hongze Depression
Jianhu Uplift
Jinhu Depression
Baiju Depression
33°
Gaoyou Depression
Qintong Depression
Haian Depression
Yellow Sea
Zhangbaling Uplift
Sunan Uplift
Yangzhou
Rugao
Yizheng
Zhenjiang
Nanjing
Yangtze River
N
km
0 20 40
32°
118°E
119°
120°
121°
Depression
Major fault
Drill core
North China Block
Yellow Sea
Tan-Lu Fault
Subei Basin
Yangtze Block
East China Sea
Cathaysia Block
South China Sea
30°N
25°
20°
110°E
115°
120°
B
Drill QY 1
(m)
Member
Era/Period/Epoch
Formation (abbreviation)
Member
Cenozoic
Quaternary
Neogene
Paleogene
Pleistocene -Holocene
Pliocene -Miocene
Oligocene
Eocene
Paleocene
Dongtai(Qd)
Yancheng(Ny)
Sanduo(E2s)
Dainan(E2d)
Funing(E1f)
Ny2
Ny1
E2s2
E2s1
E2d2
E2d1
E1f4
E1f3
E1f2
E1f1
3660
3680
3700
3720
3740
3760
3780
3800
3820
3840
3860
3880
3900
3920
3940
3960
3980
4000
4020
4040
4060
4080
Mudstone
Laminated dolomitic mudstone
Massive calcareous mudstone
Carbonate-rich layer

Fig. 1

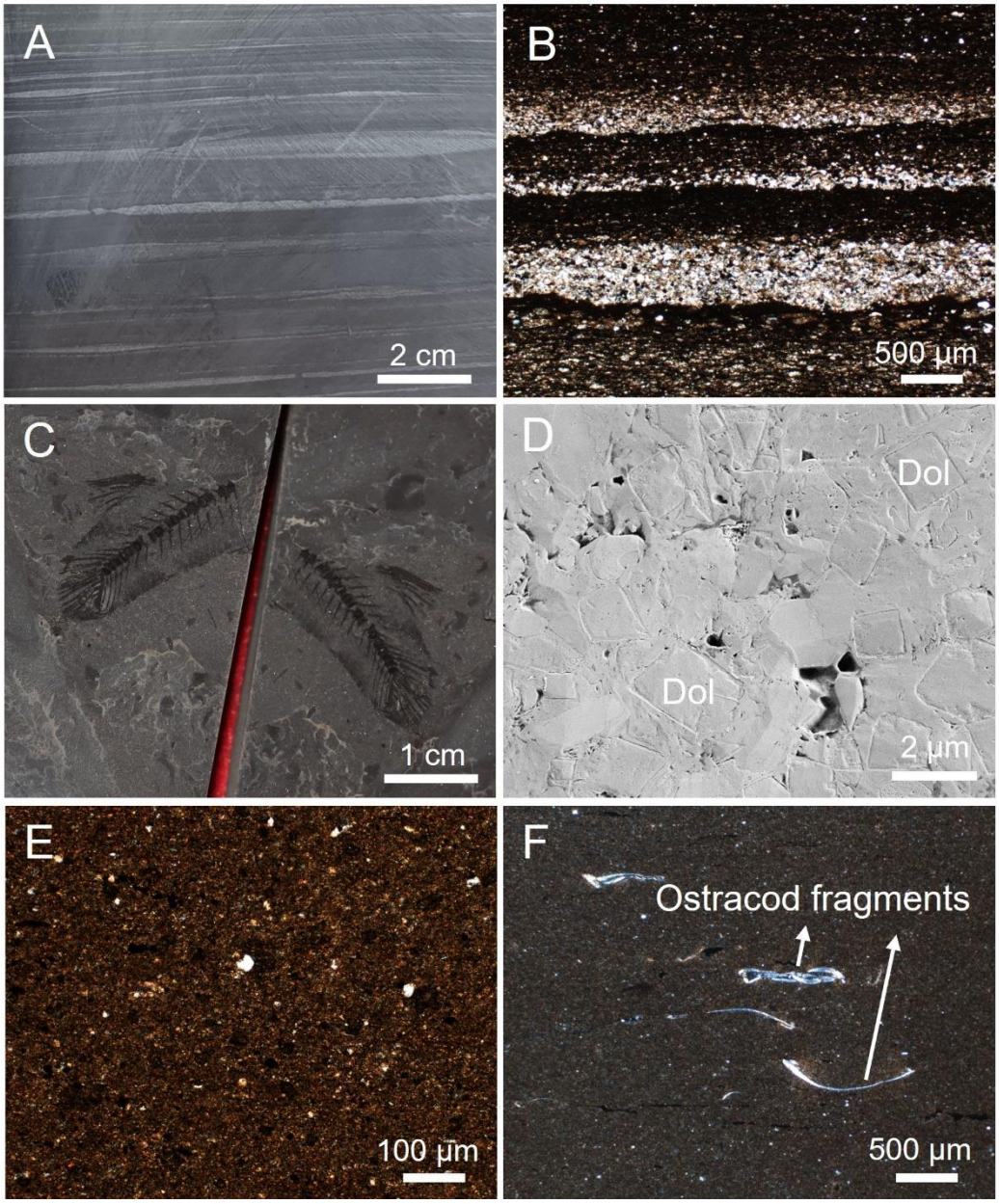
A
2 cm
B
500 µm
C
1 cm
D
Dol
Dol
2 µm
E
100 µm
F
Ostracod fragments
500 µm

Fig. 2

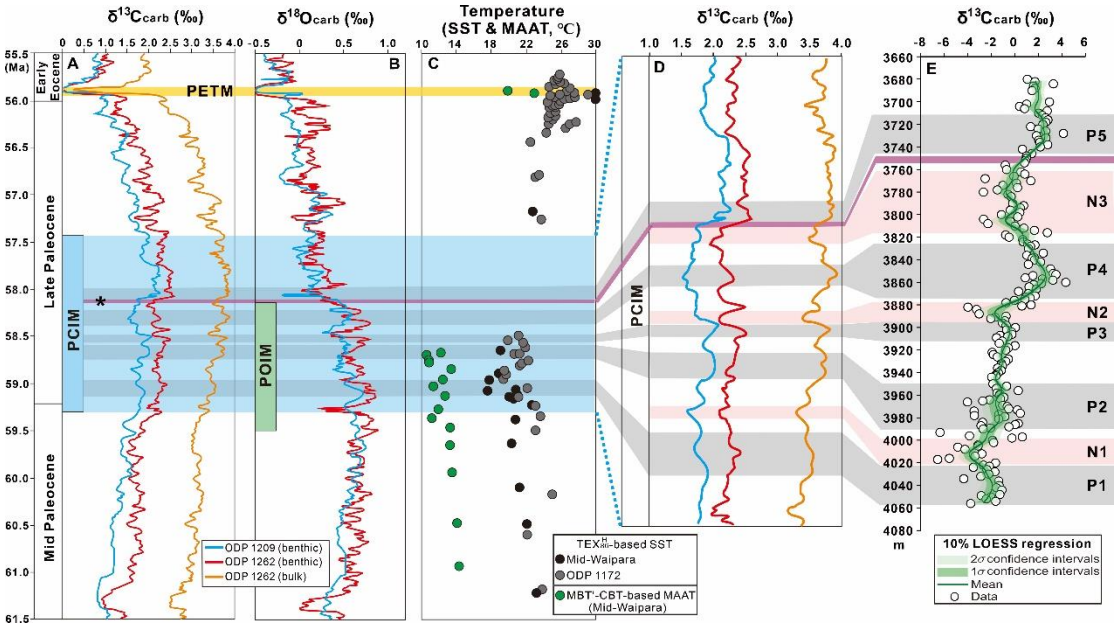
δ13Ccarb (‰)
δ18Ocarb (‰)
Temperature (SST & MAAT, °C)
δ13Ccarb (‰)
δ13Ccarb (‰)
A
B
C
D
E
PETM
PCIM
POIM
Early Eocene
Late Paleocene
Mid Paleocene
ODP 1209 (benthic)
ODP 1262 (benthic)
ODP 1262 (bulk)
TEX86H-based SST
Mid-Waipara
ODP 1172
MBT'-CBT-based MAAT (Mid-Waipara)
P5
N3
P4
N2
P3
P2
N1
P1
10% LOESS regression
2σ confidence intervals
1σ confidence intervals
Mean
Data
m

Fig. 3

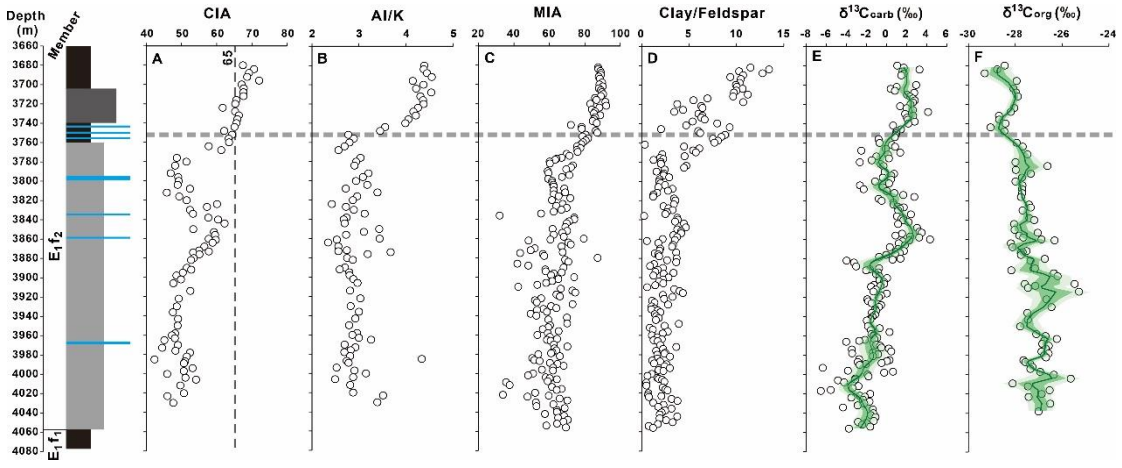
Depth (m)
Member
CIA
Al/K
MIA
Clay/Feldspar
δ13Ccarb (‰)
δ13Corg (‰)
A
B
C
D
E
F
65
E1f2
E1f1

Fig. 4

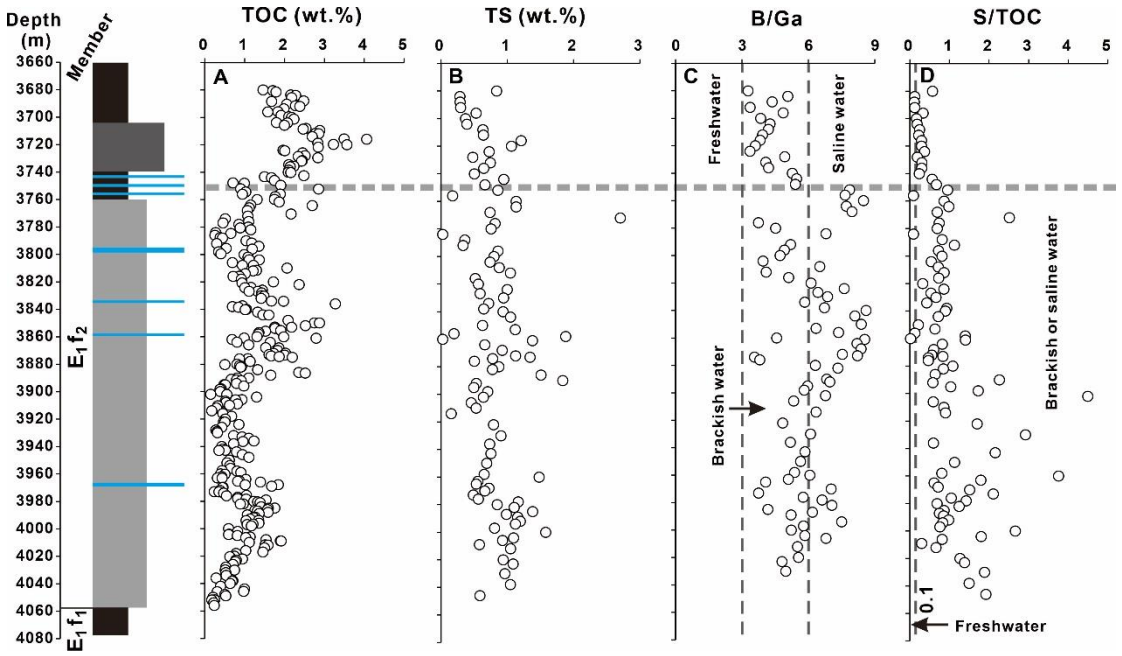
Depth (m)
Member
TOC (wt.%)
TS (wt.%)
B/Ga
S/TOC
A
B
C
D
Freshwater
Saline water
Brackish water
Brackish or saline water
0.1
Freshwater
E1f2
E1f1

Fig. 5

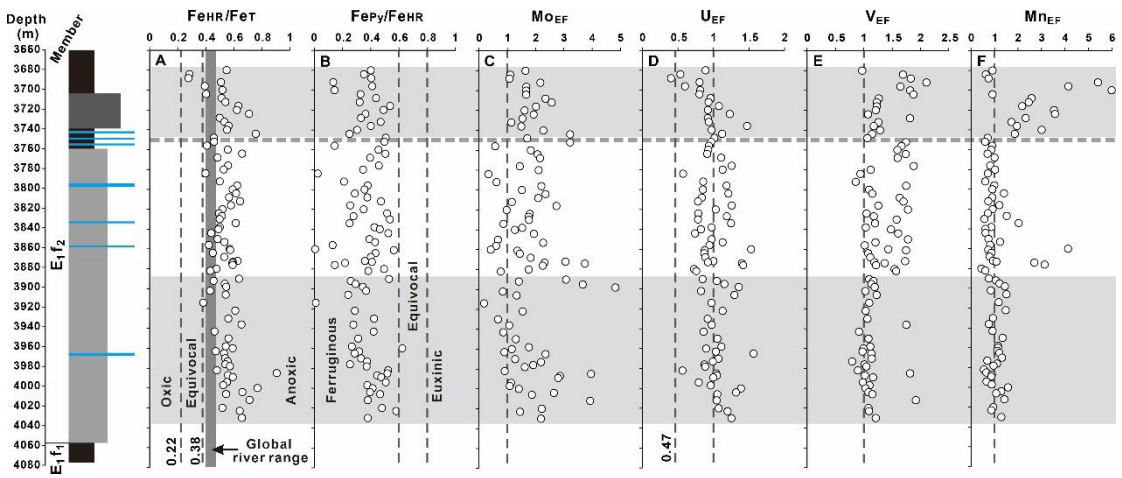
Depth (m)
Member
E_1f_2
E_1f_1
Fe_{HR}/Fe_T
Fe_{Py}/Fe_{HR}
Mo_{EF}
U_{EF}
V_{EF}
Mn_{EF}
A
B
C
D
E
F
Oxic
Equivocal
Anoxic
Ferruginous
Equivocal
Euxinic
0.22
0.38
Global river range
0.47

Fig. 6

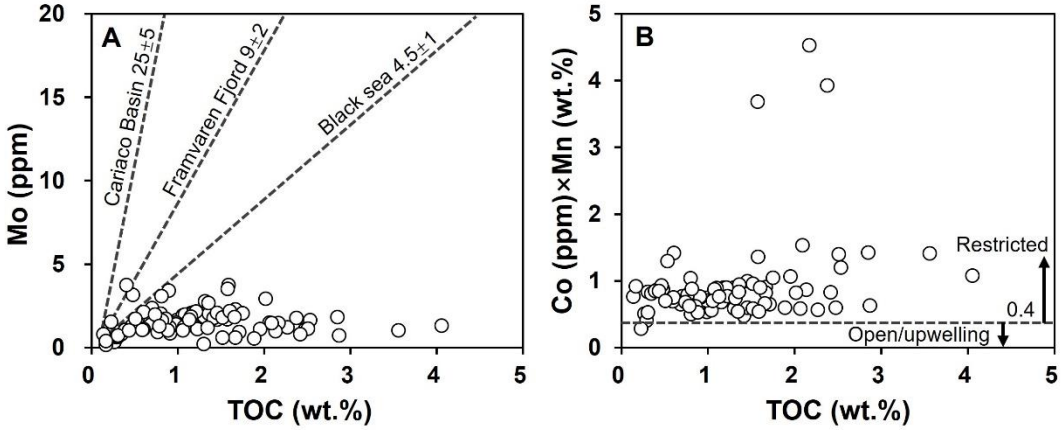
A
Mo (ppm)
TOC (wt.%)
Cariaco Basin 25±5
Framvaren Fiord 9±2
Black sea 4.5±1
B
Co (ppm)×Mn (wt.%)
TOC (wt.%)
Restricted
0.4
Open/upwelling

Fig. 7

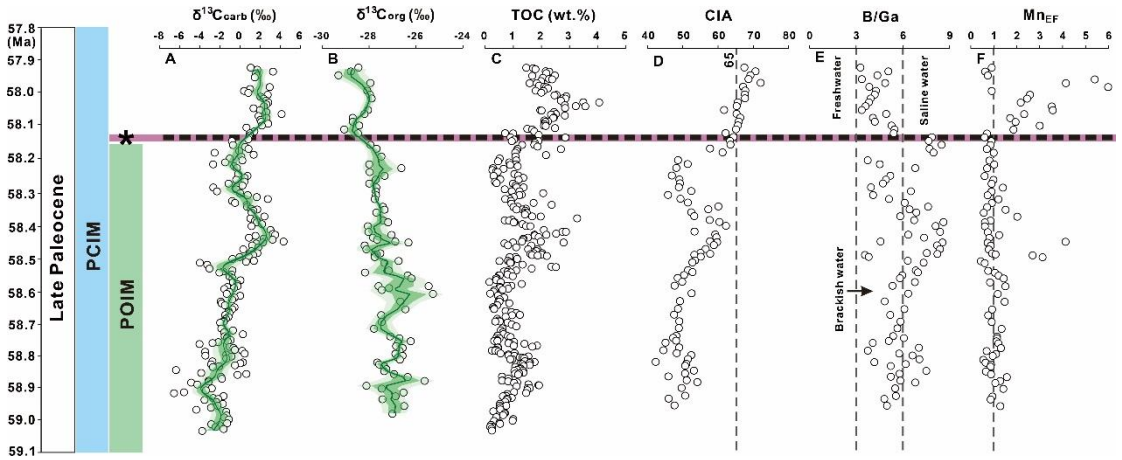
δ13Ccarb (‰)
δ13Corg (‰)
TOC (wt.%)
CIA
B/Ga
MnEF
A
B
C
D
E
F
57.8 (Ma)
57.9
58.0
58.1
58.2
58.3
58.4
58.5
58.6
58.7
58.8
58.9
59.0
59.1
Late Paleocene
PCIM
POIM
65
Freshwater
Saline water
Brackish water

Fig. 8

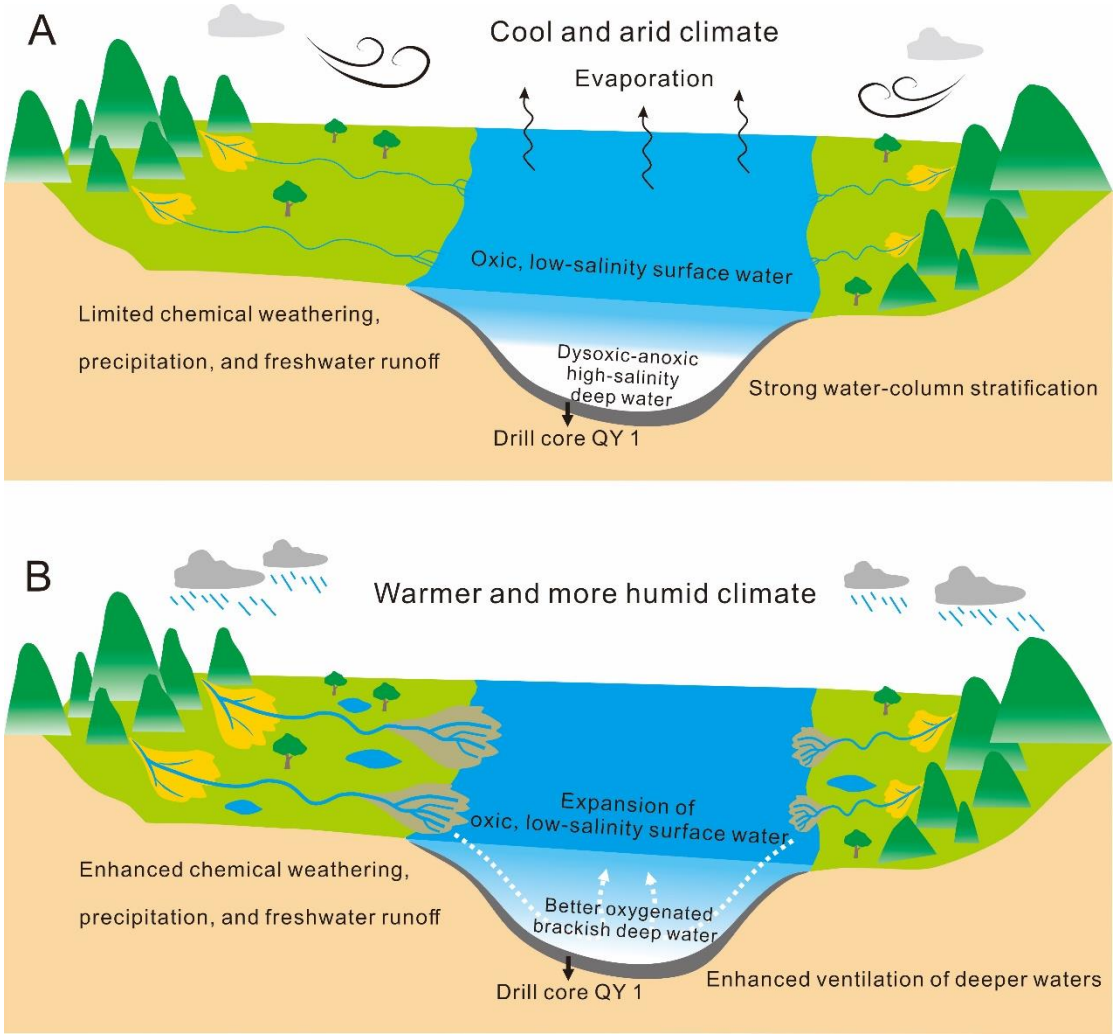
A
Cool and arid climate
Evaporation
Oxic, low-salinity surface water
Limited chemical weathering,
precipitation, and freshwater runoff
Dysoxic-anoxic
high-salinity
deep water
Strong water-column stratification
Drill core QY 1
B
Warmer and more humid climate
Expansion of
oxic, low-salinity surface water
Enhanced chemical weathering,
precipitation, and freshwater runoff
Better oxygenated
brackish deep water
Drill core QY 1
Enhanced ventilation of deeper waters

Fig. 9